RSC Advances

PAPER

View Article Online
View Journal | View Issue

Cite this: *RSC Adv.*, 2014, **4**, 26251

Aptamer based surface enhanced Raman scattering detection of adenosine using various core sizes of Au–Ag core–shell nanoparticles†

Fu-Hsiang Ko[a] and Yu-Cheng Chang*[b]

Received 28th March 2014
Accepted 6th June 2014

DOI: 10.1039/c4ra02762k

www.rsc.org/advances

The present study synthesizes different sizes of Au nanoparticles (NPs) by adjusting the concentration of citrate. This method produces Au NPs with uniform sizes that can be used to grow Au–Ag core–shell NPs by the seeding growth method. We report the fabrication of monolayer Au NPs or Au–Ag core–shell NPs through the self-assembly of NPs on a 3-aminopropyltrimethoxysilane (APTMS)-modified silicon substrate. The results indicate that the self-assembly time of Au NPs or Au–Ag core–shell NPs plays a crucial role in determining the surface coverage of NPs on the silicon substrate. The appropriate sizes of Au NPs or Au–Ag core–shell NPs were optimized to yield the greatest SERS effect in the rhodamine B molecule. The substrates with self-assembled Au–Ag core–shell NPs can also be used to detect adenosine by a structure-switch aptamer. The combination of Au–Ag core–shell NPs and DNA-based adenosine sensors provides a facile, high enhancement, low detection limit (0.1 nM) and low cost fabrication, which shall be of significant value for practical applications of other aptamer sensing systems.

1. Introduction

Surface enhanced Raman spectroscopy (SERS) is a powerful vibrational spectroscopy technique with a highly sensitive and selective application that allows for detection of chemical or biological molecules in very low concentration, and provides rich structural information.[1,2] The enhancement effect is normally described by two enhancement mechanisms. One is a long-range electromagnetic (EM) effect that results from the enhancement of the local electromagnetic field due to surface plasmon resonance of nanoscale surface roughness features in the 10–200 nm range.[3–6] The enhancement intensity is determined by many factors, such as sizes, shapes, composition, and analytic molecules adsorbed on the substrates.[7,8] The other mechanism is a chemical enhancement effect that results from the charge-transfer excitation of chemisorbed molecules.[1,7] Since its discovery, SERS has been employed as a powerful tool in the non-destructive and ultrasensitive detection of proteins, DNA, nucleic acids, glucose, and small molecules.[9–12]

Aptamers are oligonucleic acid or peptide molecules that can bind to a wide range of target molecules (proteins, drugs, and amino acids, *etc.*) with high specificity and selectivity.[13,14] Due to their high selectivity, stability, versatile target binding, and easy regeneration capabilities over traditional antibodies, aptamers have received considerable research attention as recognition ligands in biological detections.[15] Nanomaterials have recently emerged as ideal candidates enabling efficient signal transduction and amplification in aptasensors. The nanomaterial-assisted aptasensors display unprecedented advantages in sensing applications and have attracted significant consideration in other multidisciplinary studies.[12,16] Optical detection methods such as colorimetry, fluorescence, and SERS are most widely adopted for signal harvesting in aptasensors because of typical and easy approach techniques.[17] SERS provides a high sensitivity that is comparable with fluorescence detection. SERS has several intrinsic advantages over fluorometry such as fingerprints of analyses, excitation at any wavelength, alleviated photo-bleaching, narrow peak widths, and reproducibility.[1,7] The combination of SERS and nanomaterial-assisted aptasensors open up a whole new area for the application of biosensors.

The ability to develop SERS substrates with strong enhancement factors, low cost, good stability, and high reproducibility is still an important challenge.[18] Various approaches have been developed to fabricate SERS substrates, but with limited success.[19] The success of SERS is highly dependent on the interaction between adsorbed molecules and the surface of

[a]*Department of Materials Science and Engineering, National Chiao Tung University, Hsinchu, 30010, Taiwan*

[b]*Department of Materials Science and Engineering, Feng Chia University, Taichung, 40724, Taiwan. E-mail: ychang0127@gmail.com; Fax: +886-4-24510014; Tel: +886-4-24517250 ext. 5348*

† Electronic supplementary information (ESI) available: UV-vis spectra of Au NPs, EDS spectra of Au NP and Au–Ag core–shell NP, TEM images of Au–Ag core–shell NPs, dimension and self-assembly conditions of Au NPs and Au–Ag core–shell NPs, SERS intensity for rhodamine B on the different sizes of Au NPs, SERS intensity for TMR on the different core sizes of Au–Ag core–shell NPs. SERS spectra for TMR on the different sizes of Au NPs. SERS intensity for TMR on the biggest core sizes of Au–Ag core–shell NPs at the different concentration of adenosine. See DOI: 10.1039/c4ra02762k

plasmonic nanostructures. SERS substrates commonly used gold (Au), silver (Ag), or copper (Cu).[1,20] In general, Au and Ag are most often used as SERS substrates because they are air stable materials rather than Cu.[18] Compared to Ag, Au has lower enhancement factors in visible light, but it is easier to prepare as monodisperse sols in a variety of diameters.[21] By combining these two metals into a single entity, the catalytic properties can be further enhanced and the localized surface plasmon absorption can be varied continuously between the limits of the monometallic Au and Ag nanoparticles (NPs).[22,23] Recently, a strategy for extracting optical constants of the core and/or the shell material of bimetallic Au–Ag NPs from their measured surface plasmon extinction spectra was reported.[24] SERS enhancement as a function of the layered Au–Ag NP composition and the state of their aggregation was investigated using pyridine and other types of probe adsorbates.[25] However, understanding the effect of core sizes on SERS signals and the synthesis of large sizes of Au–Ag core–shell NPs without aggregation is still unclear.

The present study has successfully synthesized the different sizes of Au NPs by a modified Turkevich reaction system.[26] The concentration of citrate plays an important role in growing the different sizes of Au NPs. The Au–Ag core–shell NPs with different sizes have been synthesized by the seeding growth method. The appropriate self-assembly time can be used to control the similar surface coverage of Au NPs or Au–Ag core–shell NPs on a 3-aminopropyltrimethoxysilane (APTMS)-modified silicon substrate. Au–Ag core–shell NPs can provide a greater SERS effect on the rhodamine B molecule rather than Au NPs. The silicon substrates with self-assembled Au–Ag core–shell NPs can also be used to detect adenosine by a structures-switch aptamer. The fabrication of DNA-based adenosine sensors is facile, of high reproducibility, and low detection limit (0.1 nM), which shall be advantageous in applications for other aptamer sensing systems.

2. Experimental

2.1 Chemicals

Hydrogen tetrachloroaurate(III) trihydride, ethanol, hydrogen peroxide, adenosine, and phosphate buffered saline (PBS) were purchased from SIGMA. Silver nitrate, trisodium citrate dihydride, and sulfuric acid were purchased from J. T. Baker. 3-Aminopropyltrimethoxysilane (APTMS), rhodamine B, and 3-mercapto-1-hexanol (MCH) were purchased from Alfa Aesar. The three types of deoxyribonucleic acid (DNA) were synthesized by MDBio, Inc. All chemicals and materials were of analytical grade and used as received. De-ionized water (>18 MΩ cm^{-1}) was used throughout the experiments.

2.2 Characterization

The morphology of nanostructures was examined with a field emission scanning electron microscope (FESEM) using a JEOL JSM-6700F SEM operating at 10 kV accelerating voltage. A JEOL-2010 transmission electron microscope (TEM) operating at 200 kV was used to examine the microstructures. An electron dispersive spectrometer (EDS) attached to the TEM was used to determine the composition of NPs. A Hitachi U-2900 UV-vis spectroscopy was employed to characterize the optical properties of NPs. The Raman spectra were performed by Confocal Raman Microscope (HORIBA, LabRAM HR) at room temperature in the backscattering configuration. The source light was He–Ne laser emitting at a wavelength of 632.8 nm.

2.3 Preparation of Au NPs

The different sizes of Au NPs were synthesized by adding 1 mL of a different concentration of trisodium citrate to 10 mL aqueous solution of boiling 1 mM hydrogen tetrachloroaurate(III) trihydride under vigorous stirring. After the appearance of a wine color, boiling and stirring were continued under refluxing for 10 min and then cooled at room temperature.

2.4 Preparation of Au–Ag core–shell NPs

The 2.5 mL Au NPs with different sizes were diluted to 8 mL with de-ionized water and reheated to boil, followed by adding 1 mL of a different concentration trisodium citrate under vigorous stirring. Next, 2 mL of 5 mM silver nitrate was added, and the boiling was continued for 10 min. The Au–Ag core–shell NPs solution was cooled and stored at room temperature.

2.5 Preparation of substrate

Si (100) wafers were cleaned in a boiling piranha solution (H_2O_2–concentrated H_2SO_4, 3 : 7, v/v) for 10 min, and then rinsed with de-ionized water and ethanol. The substrates were immersed into an ethanol solution containing 5 mM APTMS and then heated under reflux for 2 h. Next, the substrates were rinsed with ethanol and de-ionized water, and then dried under a N_2 purge. The Au NPs or Au–Ag core–shell NPs were deposited onto the amino-terminated bonding by using an immersion method. After immersing the substrates in a solution of Au NPs or Au–Ag core–shell NPs for an appropriate time, the substrates were immediately rinsed with de-ionized water and dried under a N_2 purge.

2.6 Detection of adenosine

Fig. 1 depicts schematically the method used to fabricate the adenosine sensing platform. All the solutions were prepared with a PBS buffer. First, the hybridization of aptamer solution with DNA (1) (5′-AGA GAA CCT GGG GGA GTA TTG CGG AGG AAG GT-3′) and DNA (2) (3′-TAMRA-TCT CTT GGA CCC-5′, TMR-labelled DNA): the 500 μL of 1 μM DNA (1) was mixed with 500 μL of 1 μM DNA (2) and heated in a water bath at 95 °C for 10 min. This solution was cooled at room temperature and stored at 4 °C. Second, the thiolated DNA (3) (5′-SH-AGA GAA CCT GGG-3′) was modified to substrate according to the literature:[27] 20 μL of 1 μM DNA (3) was dropped onto the prepared substrate for 12 h at 4 °C. After rinsing with PBS, the substrate was immersed under 1 mM of MCH for 5 min and thoroughly rinsed. Third, the adenosine solution was diluted to various concentrations ranging from 0.1 nM to 1 μM with PBS, and then

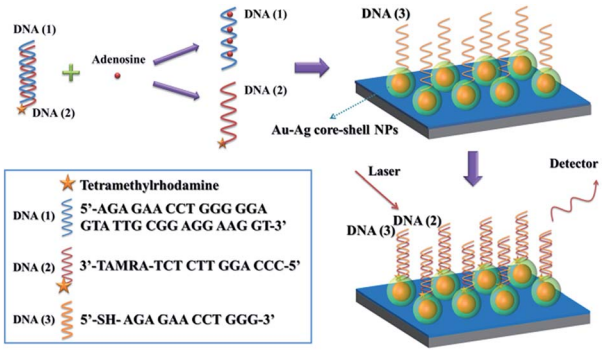

Fig. 1 Schematic diagram for preparation of sensing system for adenosine.

mixed in an aptamer solution with DNA (2) double-stranded DNA (1) with a 1 : 1 ratio. 20 μL of mixture was then dropped onto the prepared SERS substrate for 2 h. Finally, the sensing platform was washed with a PBS buffer and dried under a N_2 purge. The signal intensity of the band at 1648 cm^{-1} was recorded *versus* different concentrations of adenosine.

3. Results and discussion

3.1 Evaluation of the different sizes of Au NPs

The optical properties of Au NPs solution measured by UV-vis spectroscopy are depicted in Fig. 2a. The UV-vis spectra of Au NPs solution appear sharp and narrow. The maximum peaks are at 529, 524, 521, and 519 nm, respectively. The wavelength of maximum absorbance was decreased with the increase in concentration of citrate, as shown in Fig. 2b. The inset photos are depicted from left to right with the color change from dark wine to wine, and the concentrations of citrate at 15.5, 19.4, 25.9, and 38.8 mM, respectively. The blue shift is ascribed to the quantum confinement effect arising from the reduced sizes of the Au NPs. The role of the citrate in the growth process of Au NPs is not only reducing Au^{3+} to Au, but also controlling the sizes of the Au NPs. If the concentration of citrate is lower than 15.5 mM, the sizes of Au NPs appear non-uniform. The UV-vis spectra (Fig. S1†) exhibit a broad peak, which is attributed to the lower concentration of citrate being unable to provide for the inhibition of aggregation. The appropriate concentration of citrate can be exploited to control the different sizes of Au NPs.

The sizes of Au NPs were determined by transmission electron microscopy. The variation of concentration of citrate was found to affect the sizes of Au NPs. Fig. 2c–f show TEM images of Au NPs with spherical geometry, which were grown in citrate concentrations of 15.5, 19.4, 25.9, and 38.8 mM, respectively. The diameters of the Au NPs are 29.5, 23.4, 18.7, and 13.1 nm, respectively. The high concentration of citrate may induce the reduction in the sizes of Au NPs at the same Au precursors. On the other hand, varying the concentration of citrate led to significant changes in the sizes of Au NPs. The chemical composition of the NPs was analyzed by energy-dispersive spectroscopy (EDS). The EDS spectrum (Fig. S2†) reveals the composition of Au NP with only one gold component (Cu is from the TEM grid). Appropriate amounts of citrate led to the growth of Au NPs with different sizes.

3.2 Evaluation of the different core sizes of Au–Ag core–shell NPs

Recently, the seeding growth approach based on the temporal separation of nucleation and growth processes is considered to be a very efficient method in controlling the bimetal core–shell NPs size and shape precisely.[28] Herein, the seeding growth method can be used to synthesize Au–Ag core–shell NPs on the different sizes of Au NPs. Fig. 3a shows the UV-vis spectra of Au–Ag core–shell NPs solution with a maximum peak at the 405, 411, 416, and 420 nm, respectively. The diameters of Au NPs are 13.1, 18.7, 23.4, and 29.5 nm, respectively. The wavelength of maximum absorbance increased with the increase in the sizes of Au NPs, as shown in Fig. 3b. The inset photos are depicted

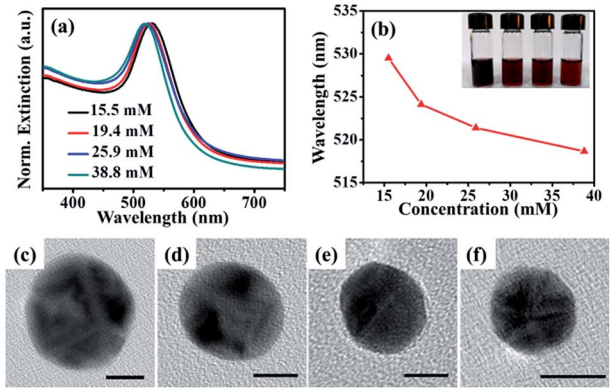

Fig. 2 (a) UV-vis spectra of Au NPs solutions synthesized in different concentrations of citrate. (b) The wavelength of Au NPs maximum absorbance as a function of the concentration of citrate. The inset image is the photo of (a). TEM images (scale bar = 10 nm) of an Au NP grown with (c) 15.5 mM, (d) 19.4 mM, (e) 25.9 mM, and (f) 38.8 mM citrate solution, respectively.

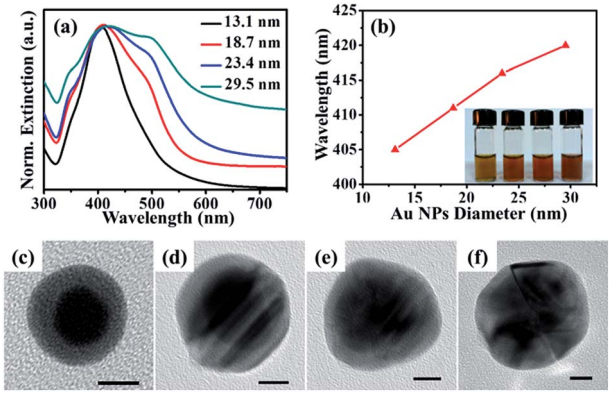

Fig. 3 (a) UV-vis spectra of Au–Ag core–shell NPs solutions synthesized on the different sizes of Au NPs. (b) The wavelength of Au–Ag core–shell NPs maximum absorbance as a function of the sizes of Au NPs. The inset image is the photo of (a). TEM images (scale bar = 10 nm) of an Au–Ag core–shell NP synthesized on the different sizes of Au NP: (c) 13.1 nm, (d) 18.7 nm, (e) 23.4 nm, and (f) 29.5 nm.

from left to right with the color change from yellow to yellow brown. The red shift is also ascribed to the quantum confinement effect arising from the increased sizes of the Au–Ag core–shell NPs. When the sizes of Au NPs solution were higher than 18.7 nm, the shoulder band of Au–Ag core–shell NPs solution became relatively evidence. The shoulder in the SPR band can be observed at around 490 nm, which seems to increase in relative intensity as compared with the sizes of Au NPs. The phenomenon is caused by the LSPR of the large Au core.

Fig. 3c–f show TEM images of an Au–Ag core–shell NP with spherical geometry and grown for the diameters of Au NPs at 13.1, 18.7, 23.4, and 29.5 nm, respectively. The TEM images clearly show that the NP with a core–shell structure and the diameters of Au–Ag core–shell NP increase from 24.8, 32.9, 43.5, and 52.9 nm, respectively. The morphology and distribution of different sizes of Au–Ag core–shell NPs can be clearly obtained by low magnification of TEM images (Fig. S3†). The EDS spectrum (Fig. S4a†) shows that the only element of Ag is present in the side of core–shell NP. In addition, the EDS spectrum (Fig. S4b†) shows that the elements of Au and Ag are present in the center of the core–shell NP. These results confirm that the constituents are the Au core and the Ag shell. The correlation between the varied sizes of Au NPs and the seeding growth approach can be exploited to control the sizes of Au–Ag core–shell NPs.

3.3 Evaluation of self-assembly Au NPs and Au–Ag core–shell NPs

The self-assembly method, which is an essential part of nanotechnology, is one of the best non-physical deposition techniques for building 2D or 3D nanostructures.[29,30] Previous studies have employed the self-assembly technique utilizing the chemical interaction between NPs and the substrate or structure surface. For instance, organic molecules containing thiol (–SH) or amine ($-NH_2$) can be adsorbed onto the gold or silver surface to form a well-organized self-assembly monolayer.[31] In our previous works, the fabrication of monolayer Au NPs was carried out using immersion or the spin coating method on a 3-aminopropyltrimethoxysilane (APTMS)-modified silicon substrate.[32] Fig. 4a illustrates the procedure used to fabricate Au NPs or Au–Ag core–shell NPs onto the silicon substrate. The fabrication processes can be briefly divided into two steps: (1) APTMS-functionalization of the silicon substrate and (2) self-assembly of Au NPs or Au–Ag core–shell NPs on APTMS. The first step deposits a large-scale monolayer APTMS on the silicon substrate with a thin native oxide layer. The second step deposits the Au NPs or Au–Ag core–shell NPs onto the amino-terminated bonding using an immersion method. After immersing the substrate in a solution of Au NPs or Au–Ag core–shell NPs for the desired time duration, the substrate is immediately rinsed with de-ionized water and dried under a N_2 purge.

Fig. 4b–e show top-view SEM images of the different sizes of Au NPs self-assembled on the Si substrate. The average diameters of Au NPs are 12.2 ± 1.8, 17.5 ± 2.7, 20.1 ± 3.5, and 26.8 ± 5.1 nm, respectively. The uniform sizes of Au NPs can be

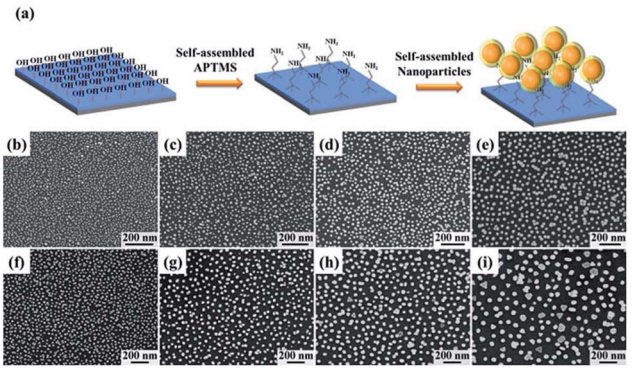

Fig. 4 (a) Schematic diagram for self-assembly NPs. The SEM images of the different sizes of Au NPs were deposited on the silicon substrate: (b) 13.1, (c) 18.7, (d) 23.4, and (e) 29.5 nm. The SEM images of the different sizes of Au–Ag core–shell NPs were deposited on the silicon substrate: (f) 24.8, (g) 32.9, (h) 43.5, and (i) 52.9 nm.

effectively controlled with the appropriate concentration of citrate as well as the growth condition. The densities and self-assembly time of Au NPs are 2356(15), 1164(30), 723(60), and 396(100) per micron^{-2} (min), respectively. In addition, the surface coverage of Au NPs can be calculated from SEM images at 27.5, 24.9, 22.9, and 22.3%, respectively. The average diameters and self-assembly conditions for the different sizes of Au NPs are listed in Table S1.† Appropriate self-assembly time leads to the growth of Au NPs with similar surface coverage. The self-assembly time progressively increases with an increase in the sizes of Au NPs. The result is attributed to decrease in the concentration of Au NPs solution.

The different sizes of Au–Ag core–shell NPs can also be self-assembled on the Si substrate, as shown in Fig. 4f–i. The average diameters of Au–Ag core–shell NPs are 23.4 ± 3.3, 30.9 ± 5.5, 38.4 ± 5.6, and 52.1 ± 8.2 nm, respectively. Compared to the average diameters of Au NPs, the average shell thicknesses of Au–Ag core–shell NPs are 5.6, 6.7, 9.2, and 12.7 nm, respectively. The shell thicknesses of Au–Ag core–shell NPs increase with an increase in sizes of Au NPs. This phenomenon is attributed to decrease in the concentration of Au NPs solution. On the other hand, the shell thicknesses of Au–Ag core–shell NPs can also be controlled by the different sizes of Au NPs. The densities and self-assembly time of Au–Ag core–shell NPs are 641(45), 336(75), 207(120), and 105(180) per micron^{-2} (min), respectively. The surface coverage of Au–Ag core–shell NPs can be calculated from SEM images at 27.6, 25.2, 24.0, and 22.4%, respectively. The average diameters and self-assembly conditions for the different core sizes of Au–Ag core–shell NPs are listed in Table S2.† In order to achieve the similar surface coverage of NPs, Au–Ag core–shell NPs require a longer self-assembly time. When the self-assembly time was longer than 180 min, the Au–Ag core–shell NPs appeared the aggregation and precipitation. This phenomenon is attributed to the occurrence of aggregation during the long self-assembly time of NPs. These results confirm that the self-assembly time plays a crucial role in determining the different sizes of Au NPs and Au–Ag core–shell NPs with similar surface coverage on the silicon

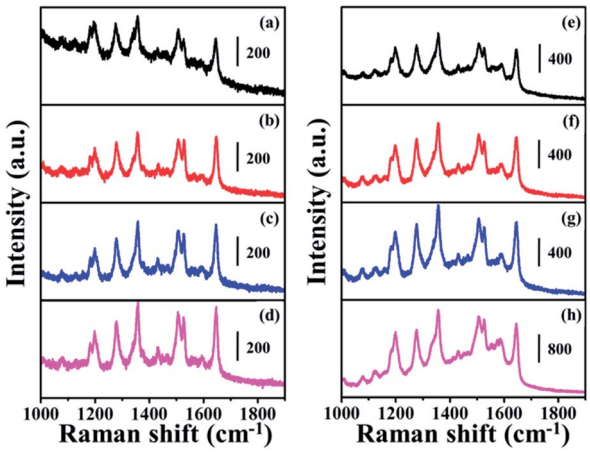

Fig. 5 SERS spectra of rhodamine B (1×10^{-6} M) absorbed on the silicon substrate with self-assembled the different sizes of Au NPs and Au–Ag core–shell NPs. Au NPs: (a) 13.1, (b) 18.7, (c) 23.4, and (d) 29.5 nm. Au–Ag core–shell NPs: (e) 24.8, (f) 32.9, (g) 43.5, and (h) 52.9 nm.

substrate. The different sizes of Au NPs and Au–Ag core–shell NPs shall be beneficial in fabricating SERS substrates.

3.4 SERS-based detection of rhodamine B

SERS effect is very sensitive to the roughness of metal surface.[1,7] Herein, the different sizes of Au NPs and Au–Ag core–shell NPs were used as substrate to examine the SERS effect. Rhodamine B was chosen as the probe molecule owing to its well-established vibrational features.[33,34] Fig. 5a–d show the SERS spectra of the rhodamine B solution (1×10^{-6} M) dispersed on the different sizes of Au NPs. The strong and medium-strong Raman bands at 1198, 1279, 1357, 1509, and 1646 cm^{-1} are observed on the nanostructure surface. The strong peaks at 1279, 1357, 1509, and 1646 cm^{-1} are assigned to the stretching modes of aromatic C–C. The band at 1198 cm^{-1} is assigned to aromatic C–H bending.[33,34] An obvious trend shows that the intensity of the Raman signals at 1646 cm^{-1} (Fig. S5†) increase gradually with an increase in the sizes of Au NPs, and the maximum SERS signals are at the sizes of 29.5 nm. The SERS spectra of the rhodamine B solution (1×10^{-6} M) are dispersed on the different sizes of Au–Ag core–shell NPs, as shown in Fig. 5e–h. For the different sizes of Au–Ag core–shell NPs, the intensity of the Raman signal at 1646 cm^{-1} also reveals similar characteristics. The SERS signals at 1646 cm^{-1} (Fig. S5†) are indeed found to increase with an increase in the sizes of Au–Ag core–shell NPs. Compared to the SERS signals at 1646 cm^{-1}, the thin Ag shell can provide for more than twice the SERS enhancement in the different sizes of Au NPs. Herein, the substrates are deposited Au NPs or Au–Ag core–shell NPs with similar surface coverage (Fig. 4). It appears that the sizes and shell thicknesses of Au–Ag core–shell NPs are the main factors affecting SERS enhancement activity at the same surface coverage. The appropriate sizes of Au–Ag core–shell NPs were optimized to yield the greatest SERS effect in the rhodamine B molecule. We believe that not only the high SERS activity of this substrate contributes to its high detection sensitivity, but also to the sorption effect of the large sizes of Au–Ag core–shell NPs, which helps to improve the detection sensitivity.

3.5 SERS-based detection of adenosine

The present study uses SERS based on a structure-switching aptamer for the detection of adenosine (Fig. 1). First, a DNA duplex is formed through the hybridization between an expanding anti-adenosine aptamer (DNA (1)) and a TMR-labelled DNA (DNA (2)). As the DNA (1)/adenosine complex is more stable than the DNA (1)/DNA (2) duplex, the DNA (1) prefer to form the DNA (1)/adenosine complex rather than the DNA (1)/DNA (2) duplex and trigger the release of DNA (2) from DNA (1)/DNA (2) duplex. Second, the silicon substrate with self-assembled the varied sizes of Au NPs or Au–Ag core–shell NPs is prepared as SERS substrate and modified with thiolated capture DNA (DNA (3)). Finally, the released DNA (2) is easily hybridized with DNA (3) on the SERS substrate, resulting in an increase in SERS signals.

Fig. 6a–d depict the SERS spectra obtained by using the aptameric sensor on the silicon substrate with self-assembled the different sizes of Au–Ag core–shell NPs at 1×10^{-4} M adenosine. SERS signals were observed with five typical Raman bands appearing in the region from 1100 to 1700 cm^{-1}. The peaks of these Raman bands are located at 1215, 1351, 1510, 1533, and 1648. The strong peaks at 1351, 1510, 1533, and 1648 cm^{-1} are assigned to the stretching modes of aromatic C–C. The band at 1215 cm^{-1} is assigned to aromatic C–H bending.[16] Although the overall SERS signals of TMR show a similar increase in the response to the target, the band at 1648 cm^{-1} was chosen as the marker band for TMR due to its ideal peak profile. The Raman intensity at 1648 cm^{-1} (Fig. S6†) obtained from the different sizes of Au–Ag core–shell NPs. It is clearly observed that the signals increase with an increase in the sizes of the Au–Ag core–shell NPs. The largest Au–Ag core–shell NPs have the maximum SERS signals. The SERS enhancement factor (EF) of the largest Au–Ag core–shell NPs is about 5.4 times

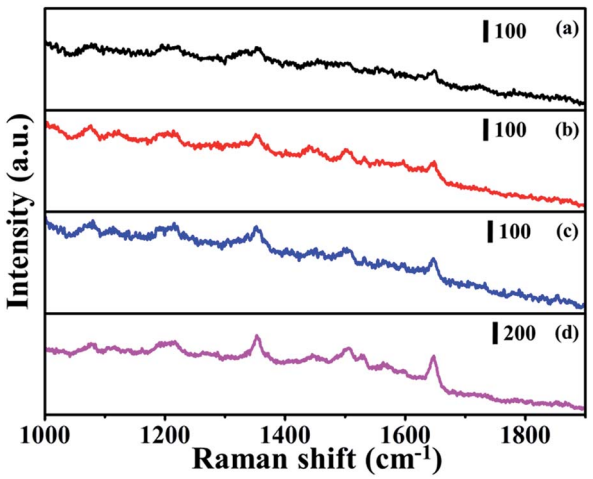

Fig. 6 SERS spectra of the aptameric sensor on the silicon substrate with self-assembled the different sizes of Au–Ag core–shell NPs at 1×10^{-4} M adenosine: (a) 24.8, (b) 32.9 (c) 43.5, and (d) 52.9 nm.

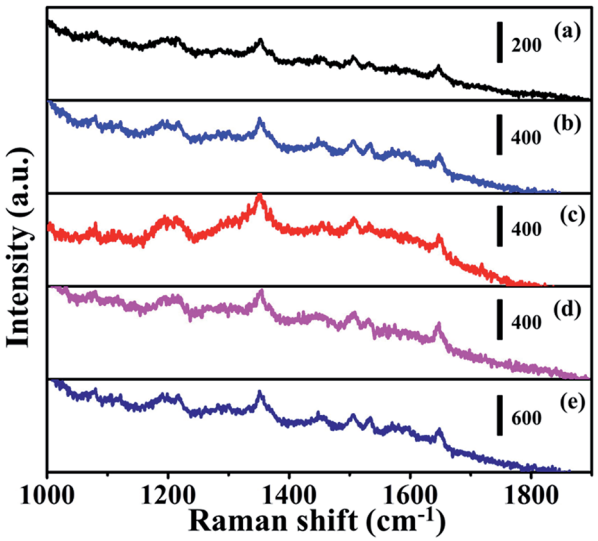

Fig. 7 SERS spectra of the aptameric sensor on the silicon substrate with self-assembled the largest sizes of Au–Ag core–shell NPs at the different concentrations of adenosine: (a) 0.1 nM, (b) 1 nM (c) 10 nM (d) 100 nM, and (e) 1 μM.

compared to the smallest. This indicates that the Au–Ag core–shell NPs as SERS substrates provided strong Raman signals of TMR.

The SERS spectra (Fig. S7†) obtained by using the aptameric sensor on the silicon substrate with the different sizes of Au NPs at 1×10^{-4} M adenosine. The SERS spectra reveal no Raman peak at 1648 cm^{-1}. The Au NPs detection schemes were limited by the complex sample preparation and relatively low enhancement factors compared Ag NPs.[35] Results indicate that the Ag shell of Au–Ag core–shell NPs plays a crucial role in aptameric sensor. Fig. 7a–e depict the SERS spectra obtained by using the aptameric sensor on the silicon substrate with self-assembled the largest sizes of Au–Ag core–shell NPs at the different concentration of adenosine. For the different concentration of adenosine, the intensity of the Raman signal at 1648 cm^{-1} reveals similar characteristics. The SERS signals at 1648 cm^{-1} (Fig. S8†) are indeed found to increase with an increase in the concentration of adenosine. The peak remains clearly observable in the adenosine solution with concentrations as low as 0.1 nM. This indicates that the Au–Ag core–shell NPs as SERS substrates provided strong Raman signals of TMR. The fabrication of DNA-based adenosine sensors is facile, of high reproducibility, and a low detection limit (0.1 nM), which shall be advantageous in applications for other aptamer sensing systems.

4. Conclusions

In summary, the Au NPs with the different sizes can be synthesized by adjusting the concentration of citrate in an aqueous solution. The different sizes of Au NPs can also be used to grow Au–Ag core–shell NPs by the seeding growth method. The appropriate self-assembly time can be used to control the densities of Au and Au–Ag core–shell NPs with similar surface coverage on an APTMS-modified silicon substrate. The largest Au–Ag core–shell NPs are beneficial in yielding the greatest SERS effect of the rhodamine B molecule on the similar surface coverage. The optimizing substrate also exhibits the best enhancement for the detection of adenosine by a structures-switch aptamer. This aptameric SERS sensor is simple and can detect adenosine as low as 0.1 nM. The SERS-based sensing system continues to have great potential for multiplex and sensitive determination in biochemical and biomedical studies.

Acknowledgements

This study was supported financially by the National Science Council, Taiwan (NSC 102-2218-E-035-009).

References

1 B. Sharma, R. R. Frontiera, A.-I. Henry, E. Ringe and R. P. Van Duyne, *Mater. Today*, 2012, **15**, 16–25.
2 J. P. Camden, J. A. Dieringer, J. Zhao and R. P. Van Duyne, *Acc. Chem. Res.*, 2008, **41**, 1653–1661.
3 V. M. Shalaev and A. K. Sarychev, *Phys. Rev. B: Condens. Matter Mater. Phys.*, 1998, **57**, 13265–13288.
4 M. Kahl and E. Voges, *Phys. Rev. B: Condens. Matter Mater. Phys.*, 2000, **61**, 14078–14088.
5 A. D. McFarland, M. A. Young, J. A. Dieringer and R. P. Van Duyne, *J. Phys. Chem. B*, 2005, **109**, 11279–11285.
6 P. Etchegoin, L. F. Cohen, H. Hartigan, R. J. C. Brown, M. J. T. Milton and J. C. Gallop, *J. Chem. Phys.*, 2003, **119**, 5281–5289.
7 M. Rycenga, C. M. Cobley, J. Zeng, W. Li, C. H. Moran, Q. Zhang, D. Qin and Y. Xia, *Chem. Rev.*, 2011, **111**, 3669–3712.
8 I. Yoon, T. Kang, W. Choi, J. Kim, Y. Yoo, S.-W. Joo, Q. H. Park, H. Ihee and B. Kim, *J. Am. Chem. Soc.*, 2008, **131**, 758–762.
9 J. Ni, R. J. Lipert, G. B. Dawson and M. D. Porter, *Anal. Chem.*, 1999, **71**, 4903–4908.
10 L. Fabris, M. Dante, G. Braun, S. J. Lee, N. O. Reich, M. Moskovits, T.-Q. Nguyen and G. C. Bazan, *J. Am. Chem. Soc.*, 2007, **129**, 6086–6087.
11 Y. Wang and J. Irudayaraj, *Chem. Commun.*, 2011, **47**, 4394–4396.
12 J.-W. Chen, X.-P. Liu, K.-J. Feng, Y. Liang, J.-H. Jiang, G.-L. Shen and R.-Q. Yu, *Biosens. Bioelectron.*, 2008, **24**, 66–71.
13 M. You, Y. Chen, L. Peng, D. Han, B. Yin, B. Ye and W. Tan, *Chem. Sci.*, 2011, **2**, 1003–1010.
14 R. Jenison, S. Gill, A. Pardi and B. Polisky, *Science*, 1994, **263**, 1425–1429.
15 Y. Xiang, X. Qian, B. Jiang, Y. Chai and R. Yuan, *Chem. Commun.*, 2011, **47**, 4733–4735.
16 J. Chen, J. Jiang, X. Gao, G. Liu, G. Shen and R. Yu, *Chem.–Euro. J.*, 2008, **14**, 8374–8382.
17 G. Wang, Y. Wang, L. Chen and J. Choo, *Biosens. Bioelectron.*, 2010, **25**, 1859–1868.

18 M. Fan, G. F. S. Andrade and A. G. Brolo, *Anal. Chim. Acta*, 2011, **693**, 7–25.
19 L. Chen, L. Luo, Z. Chen, M. Zhang, J. A. Zapien, C. S. Lee and S. T. Lee, *J. Phys. Chem. C*, 2009, **114**, 93–100.
20 M. E. Stewart, C. R. Anderton, L. B. Thompson, J. Maria, S. K. Gray, J. A. Rogers and R. G. Nuzzo, *Chem. Rev.*, 2008, **108**, 494–521.
21 H. Ko, S. Singamaneni and V. V. Tsukruk, *Small*, 2008, **4**, 1576–1599.
22 J.-H. Liu, A.-Q. Wang, Y.-S. Chi, H.-P. Lin and C.-Y. Mou, *J. Phys. Chem. B*, 2004, **109**, 40–43.
23 P. Mulvaney, *Langmuir*, 1996, **12**, 788–800.
24 M. Moskovits, I. Srnova-Sloufova and B. Vlckova, *J. Chem. Phys.*, 2002, **116**, 10435–10446.
25 R. G. Freeman, M. B. Hommer, K. C. Grabar, M. A. Jackson and M. J. Natan, *J. Phys. Chem.*, 1996, **100**, 718–724.
26 J. Turkevich, P. C. Stevenson and J. Hillier, *Discuss. Faraday Soc.*, 1951, **11**, 55–75.
27 R. Levicky, T. M. Herne, M. J. Tarlov and S. K. Satija, *J. Am. Chem. Soc.*, 1998, **120**, 9787–9792.
28 Z.-j. Jiang and C.-y. Liu, *J. Phys. Chem. B*, 2003, **107**, 12411–12415.
29 F.-K. Liu, P.-W. Huang, Y.-C. Chang, F.-H. Ko and T.-C. Chu, *Langmuir*, 2005, **21**, 2519–2525.
30 V. Chechik, R. M. Crooks and C. J. M. Stirling, *Adv. Mater.*, 2000, **12**, 1161–1171.
31 F.-K. Liu, Y.-C. Chang, F.-H. Ko, T.-C. Chu and B.-T. Dai, *Microelectron. Eng.*, 2003, **67–68**, 702–709.
32 T.-H. Chang, Y.-C. Chang, F.-K. Liu and T.-C. Chu, *Appl. Surf. Sci.*, 2010, **256**, 7339–7343.
33 M. Volný, A. Sengupta, C. B. Wilson, B. D. Swanson, E. J. Davis and F. Tureček, *Anal. Chem.*, 2007, **79**, 4543–4551.
34 T. Z. Melvin, L. Kirsty, W. Ngo-Yin, M. Hong and K. Y. J. Alex, *Nanotechnology*, 2007, **18**, 455301.
35 R. J. Stokes, A. Macaskill, P. J. Lundahl, W. E. Smith, K. Faulds and D. Graham, *Small*, 2007, **3**, 1593–1601.